Applied Physics Letters

Scanning microwave imaging of optically patterned $Ge_2Sb_2Te_5$

Cite as: Appl. Phys. Lett. **114**, 093106 (2019); https://doi.org/10.1063/1.5052018
Submitted: 13 August 2018 . Accepted: 18 February 2019 . Published Online: 08 March 2019

Scott R. Johnston, Edwin Ng, Scott W. Fong, Walter Y. Mok, Jeongwon Park, Peter Zalden, Anne Sakdinawat, H.-S. Philip Wong, Hideo Mabuchi, and Zhi-Xun Shen

AIP Publishing

Applied Physics Letters ARTICLE scitation.org/journal/apl

Scanning microwave imaging of optically patterned $Ge_2Sb_2Te_5$

Cite as: Appl. Phys. Lett. **114**, 093106 (2019); doi: 10.1063/1.5052018
Submitted: 13 August 2018 · Accepted: 18 February 2019 ·
Published Online: 8 March 2019

Scott R. Johnston,[1] Edwin Ng,[1] Scott W. Fong,[2] Walter Y. Mok,[3] Jeongwon Park,[3,4] Peter Zalden,[3,5] Anne Sakdinawat,[3] H.-S. Philip Wong,[2] Hideo Mabuchi,[1] and Zhi-Xun Shen[1,6,a)]

AFFILIATIONS

[1]Department of Applied Physics, Stanford University, Stanford, California 94305, USA
[2]Department of Electrical Engineering, Stanford University, Stanford, California 94305, USA
[3]SLAC National Accelerator Laboratory, 2575 Sand Hill Road, Menlo Park, California 94025, USA
[4]School of Electrical Engineering and Computer Science, University of Ottawa, Ottawa, Ontario K1N 6N5, Canada
[5]European XFEL, Holzkoppel 4, 22869 Schenefeld, Germany
[6]Department of Physics, Stanford University, Stanford, California 94305, USA

[a)]**Electronic mail:** zxshen@stanford.edu

ABSTRACT

The measurement of inhomogeneous conductivity in optically crystallized, amorphous $Ge_2Sb_2Te_5$ (GST) films is demonstrated via scanning microwave impedance microscopy (MIM). Qualitative consistency with expectations is demonstrated in spots crystallized by focused coherent light at various intensities, exposure times, and film thicknesses. The characterization of process imperfections is demonstrated when a mask is used to optically pattern the nanoscale features of crystalline GST in the amorphous film. These measurements show the ability of MIM to resolve partial crystallization, patterning faults, and other details in optically patterned GST.

Phase change materials (PCMs), as we refer to them here, are a class of materials which can be repeatedly switched between amorphous and crystalline phases, typically by heating. Of interest are those materials which show significant differences in electrical and optical properties between these phases. Such materials are widely applied in electrical[1] and optical storage[2] and emerging applications in displays[3] and photonics.[4,5]

The mechanism of operation is the ability to crystallize the material by maintaining an elevated temperature above the crystallization temperature, T_x, but below the melting temperature T_m. This results in transformation to the high-conductivity, high-reflectivity crystalline phase. To reset the device, the temperature is brought past the melting point, which destroys all crystalline order, and then quickly cooled to prevent recrystallization.[6]

Scanning microwave impedance microscopy (MIM) is a unique tool for the nanoscale characterization of PCMs due to its high spatial resolution (below 50 nm) and ability to measure changes in conductivity without direct electrical contact.[7] For comparison, spatially resolved x-ray diffraction is capable of directly resolving the amorphous vs. crystalline phases in PCMs, but typical spatial resolution is limited to 100s of nm.[8] Optical microscopy has similar spatial resolution limits due to diffraction. Tools such as scanning electron microscopy and atomic force microscopy (AFM) are capable of observing the topographical changes resulting from the reduced density of the amorphous phase, but they do not directly measure the quantities of interest such as crystallinity or conductivity. The remarkable results have been shown using conductive AFM in related systems;[9] however, the need for direct electrical conduction through the region of interest requires not only a counter electrode directly connected to crystalline regions but typically also the destruction of the device to access subsurface regions. Finally, for very thin devices, transmission electron microscopy can provide exquisite results.[10] This requires intensive and typically destructive sample preparation, however.

The existing method most similar to MIM for PCM characterization is scattering-type scanning optical near-field microscopy (s-SNOM).[11] Like MIM, s-SNOM is a tip-based near-field microscopy technique, and like MIM, s-SNOM measures the (complex) sample permittivity near the tip. The most important difference is the frequency of operation (optical rather than microwave). Because of this difference, s-SNOM probes the optical permittivity most directly relevant to optical applications of PCMs, such as photonic devices, while MIM probes the GHz conductivity and permittivity more relevant to electronic devices.

Sputtering was used to grow 20–100 nm films of $Ge_2Sb_2Te_5$ (GST) on poorly doped, 500 μm thick silicon (100) wafers. We used an alloy target and an argon atmosphere with a growth rate of approximately 0.1 nm/s.

Small spots of the amorphous GST films were crystallized using focused laser light at 532 nm, using an acousto-optic modulator (AOM) to control exposure time and a variable attenuator to control the incident optical power. The beam was focused by an objective into a Gaussian-intensity spot approximately 5.2 μm in $1/e^2$ diameter at the surface of the film. Additional information on patterning can be found in supplementary material B. The result is the array of dots as shown in Fig. 1(a).

Due to the significant change in optical permittivity and absorption between crystalline (x-) and amorphous (a-) GST,[12] it is possible to observe the crystallized regions of the film by standard top-illuminated optical microscopy, as shown in Fig. 1(a). On the vertical axis of Fig. 1(a), the total incident optical power is varied. With increasing power, the area which reaches T_x increases, primarily due to the Gaussian (rather than flat-top) profile of the optical spot. Lateral heat transfer is minimal because the film is much thinner than the spot size, and the Si substrate is far more thermally conductive than the GST film, acting as a good thermal ground; a thermal simulation can be found in Fig. 2(f). At sufficiently large powers (e.g., 420 mW for the 40 nm film), damage occurs at the film surface, visible as a dramatic drop in optical reflectivity and pitting in the topography.

On the horizontal axis of Fig. 1(a), we have exposure time. All exposures are relatively long compared to the 60 ns measured 90% rise/fall time for the AOM, which in turn is long compared with the 20 ns 90% thermal rise time near the film surface of the 100 nm film, as determined by simulations using instantaneous optical rise times. Thus, for all measured exposure times, the system reaches thermal

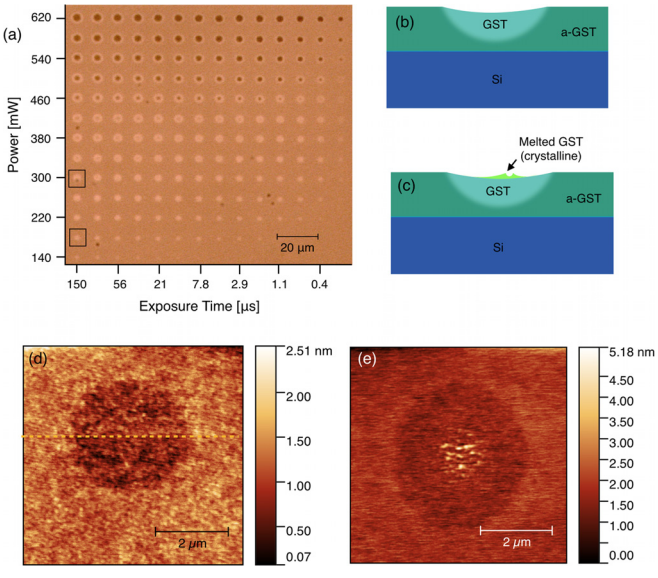

FIG. 1. (a) Optical microscopy image of the optically patterned 40 nm a-GST film. (b) Illustration of the crystallized region created by low-power patterning. (c) Illustration of melting at higher power. (d) and (e) AFM topography measurements at 180 mW, 300 mW, and 150 μs, as marked in (a).

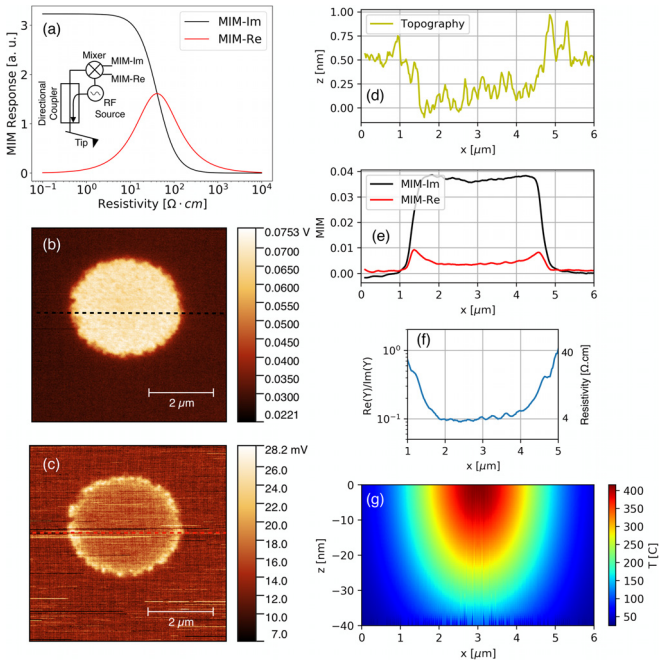

FIG. 2. (a) Calculated MIM response to changes in sample resistivity for $\epsilon_r = 35$ and (inset) simplified MIM schematic. (b) and (c) MIM-Im and MIM-Re images of the dot shown in Fig. 1(d) (180 mW, 150 μs). (d) and (e) Topography, MIM-Im, and MIM-Re linecuts. (f) MIM-Re to MIM-Im ratio gives approximate conductivity. (g) Simulation of steady-state sample temperature over a similar linecut for the same power. Note the different scaling on the vertical and horizontal axes.

equilibrium. We believe that, given the long exposure times used, the variation in spot size over exposure at fixed power is primarily due to the time needed for crystallization to occur at fixed temperature.[13] Further information is included in supplementary material C. This results in the cooler edge regions only crystallizing at long exposure times.

Turning to topography measured by AFM in Figs. 1(d) and 1(e), the crystalline dots have slightly depressed topography (e.g., 0.4 nm for the 40 nm film). This results from the higher density of the crystalline phase. A cross-section illustration of the system is shown in Fig. 1(b). Notably, this 1% depression is significantly smaller than the 6% density change reported in the literature.[14,15] We reconcile this difference by hypothesizing that the crystalline layer is significantly thinner than the full film thickness. This is supported by the thermal simulations (Fig. 3), which show that the bottom of the film does not reach crystallization temperature due to the high thermal conductivity of the silicon substrate. It is also likely that the surface oxide layer described subsequently reduces the thickness of the film which crystallizes.

One additional feature, which is not readily visible optically, is the melting of the film surface at sufficiently high powers (e.g., at 300 mW for the 40 nm film). Because the cooling is slow (limited by fall time of the AOM), the melted region also crystallizes. This is supported by the MIM measurement in supplementary material A. The bare film allows the melted region to coalesce into droplets, which are then visible in topography [Fig. 1(e)] and illustrated in Fig. 1(c).

The MIM measurement was conducted simultaneously with the topography measurement on a commercial Park Systems AFM with

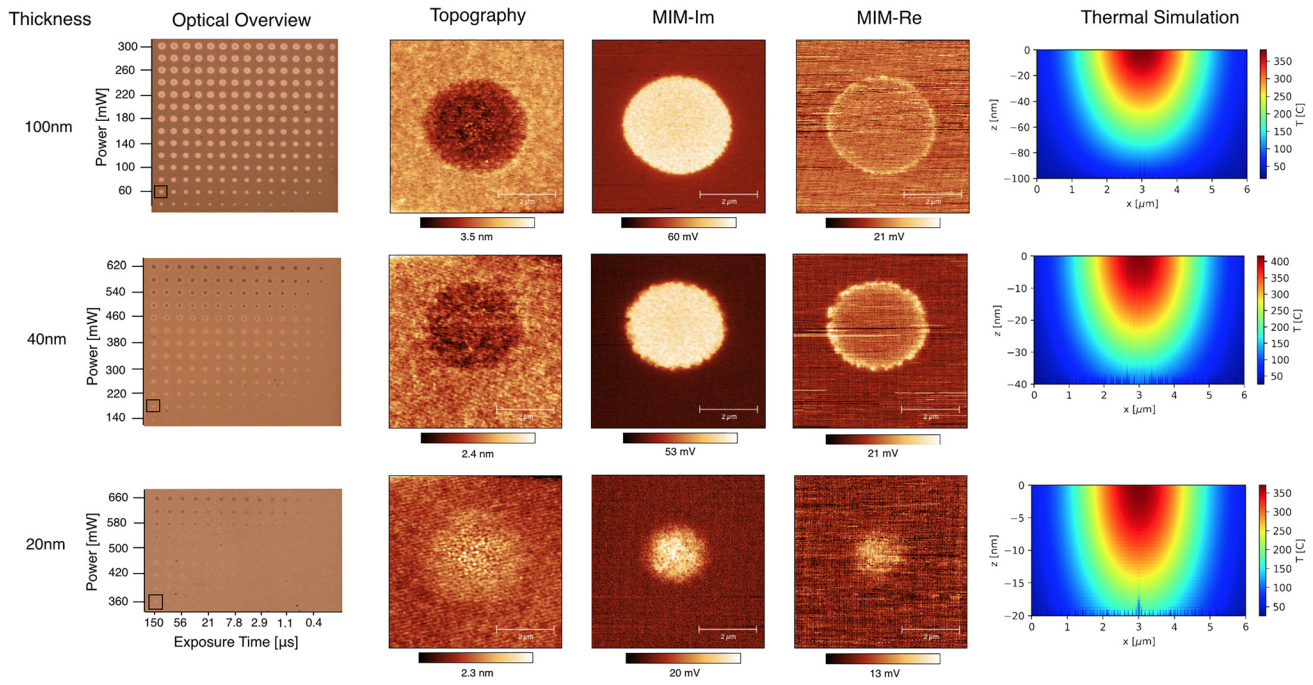

FIG. 3. 100 nm, 40 nm, and 20 nm GST films as characterized by optical microscopy, AFM topography, MIM, and thermal simulation. The spot chosen for the measurement, and simulation is indicated by a box in the optical microscopy images.

custom shielded cantilever probes,[16] tip holder, and microwave electronics. MIM provides information about local conductivity, allowing fine examination of the state of the phase change material with nanoscale resolution.

MIM measures changes in complex tip impedance, resulting from the sample under the tip apex. The tip impedance is recorded by precisely measuring the microwave signal reflected from the tip through a matching network attached nearby to the AFM head. The reflection measurement is conducted through a directional coupler and mixer-based synchronous demodulation,[17] as shown in the inset in Fig. 2(a). The sample conductivity to tip impedance, given the measurement frequency (1.25 GHz) and sample permittivity at this frequency ($\epsilon_r = 35$),[18] is also shown in Fig. 2(a). As plotted, dissipation (MIM-Re) peaks around 40 Ω cm, while capacitance (MIM-Im) increases monotonically with conductivity. The sensitivity window, ranging over roughly 0.3 Ω cm to 3000 Ω cm, covers much of the range of conductivities in GST.[19]

Figure 2(b) shows that the MIM-Im response increases dramatically over the crystallized region, as expected due to the large increase in conductivity. This large signal, as compared with the relatively subtle shift in topography, can be useful for imaging smaller features that may not be clearly visible in topography, as shown in Fig. 4. It may also be useful in other sample structures, such as thinner or buried films, where the topography change is even smaller.

The MIM-Re signal in Fig. 2(c) provides additional resolution into the degree of crystallization, or more directly the conductivity, of each point within the spot. The material around the edge of the spot is cooler than that in the center during patterning due to the Gaussian intensity profile, resulting in a partially crystallized material of intermediate conductivity near the edge. The linecuts in Fig. 2(e) precisely show the variation of the MIM channels across the dot. Furthermore, the ratio of the two can be used to estimate local conductivity, as shown in Fig. 2(f). This is because, assuming constant permittivity (which is not strictly true in this system), the ratio of MIM-Re to MIM-Im is proportional to conductivity, with the conversion depending on the MIM frequency and material permittivity. There are many caveats, in addition to non-constant permittivity, which make this only a rough estimation; the choice of offset for MIM-Im and MIM-Re shifts the overall curve up and down, primarily at larger conductivities, which is why the area outside the dot has been excluded. Furthermore, this gives a single value of conductivity for the material under the tip, whereas in practice, the material in the small region can be inhomogeneous, particularly in the z direction.

To better understand the measurement of dissipation, MIM-Re, we refer to the simulated temperature during patterning [Fig. 2(f)]. Note that there is some partially crystallized material buried underneath the crystallized material in the center of the spot since these regions also reach intermediate temperatures. Many phenomena prevent the dissipation of this material from being measured nearly as prominently as at the spot edge, however; to begin with, the conductive material over it effectively shields it from the microwave probe. Note that we model the system quasi-statically, and the shielding we describe is primarily DC shielding. That is, the field still penetrates; however, the field shape is changed. In addition, the thickness of the partially crystallized layer decreases towards the center of the spot, where more temperature is dropped over the same vertical distance.

Finally, MIM is simply less sensitive to more deeply buried layers, with almost no signal from over about 100 nm into the sample, with this sensitivity depth proportional to tip size.

The thermal simulations are produced by finite element analysis at thermally long timescales after the optical heating is applied (200 ns). An optical penetration depth of 15 nm is used based on the optical absorptivity of GST at 532 nm.[20] A thermal conductivity of 0.2 W m^{-1} K^{-1} (Ref. 21) and a thermal boundary resistance (TBR) of 30 m^2 K/GW (Ref. 22) are used. This TBR is equivalent to just 6 nm of additional a-GST.

Changes in material properties due to the phase change (reflectivity and thermal conductivity) are not taken into account. Assuming that lateral heat transfer is negligible due to the large spot size relative to film thickness, the thermal conductivity of the crystalline region will not significantly affect the temperature in the amorphous regions of the sample and thus will not alter how large a region crystallizes. This is explained further in supplementary material C. The increase in reflectivity should reduce the thickness of the crystalline region slightly as compared with our simulation, as is manifested in the small (relative to film thickness), flat depression in topography.

The thermal simulations are consistent with a T_x around 150 °C (Ref. 23) and the spot sizes observed in the 100 nm and 40 nm films, as shown in Fig. 3.

We patterned, imaged, scanned, and simulated three different thicknesses of GST on Si: 100 nm, 40 nm, and 20 nm. The results are displayed in Fig. 3. Relatively little changes between the 100 nm and 40 nm films, with the difference in power necessary to achieve similar results, accurately predicted by simulation. The dissipation near the edge of 100 nm is slightly less spread out than that for the 40 nm sample. This is likely due to the fact that in the thinner film, the dissipative layer stays closer to the surface, reducing both the amount of shielding over it and the distance from the tip.

A striking difference occurs when we switch to the 20 nm film. The optical contrast is much smaller than for the thicker films, and the topography is raised and shows the signs of melting even at the lowest power with observable contrast (Fig. 3). MIM contrast shows much lower conductivities than fully crystallized GST. The optical image of the exposure/power array shows that contrast without damage is only achieved for exposures of over 10 μs; otherwise, no contrast is achieved even at powers where we would expect crystallization to occur. We believe that this difficulty in crystallizing the 20 nm film arises from the oxidation of the top ≈10 nm of the film, which was stored at ambient conditions for an extended period.[24] One possible explanation for the small changes in conductivity and topography which do occur at very long time-scales is stoichiometric phase separation, which begins at a similar timescale.[25] Another is the delamination of the film from the substrate when the substrate is allowed to heat sufficiently, which would allow for some crystallization of the less oxidized bottom of the film only after good thermal contact with the substrate is broken.

For the sample studied in this section, a mask is used to pattern sub-wavelength features onto the GST. The GST film before patterning is identical to those in the previous paragraphs. The intended application is for use as a repatternable diffraction grating.[26] The sample overview can be seen in Fig. 4(a), although a larger feature size (600 nm pitch) is used for this image, as it is more readily seen under the microscope.

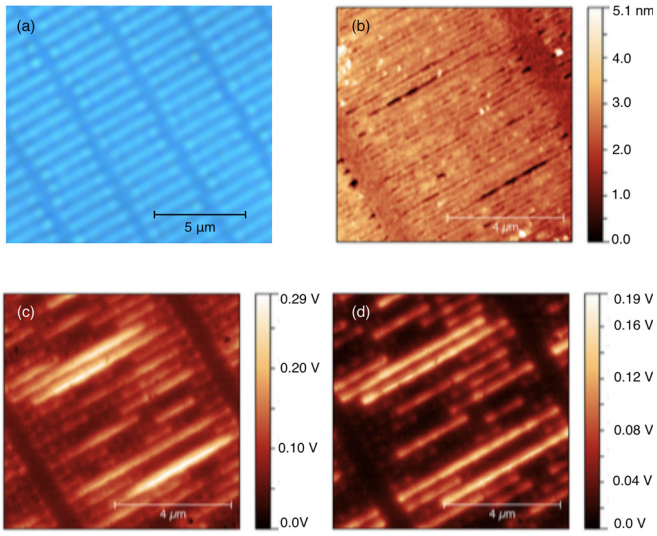

FIG. 4. (a) Optical image of the 600 nm pitch optically patterned GST grating. (b) Topography, (c) MIM-Im, and (d) MIM-Re of the 400 nm pitch grating [different samples from (a)]. Note the irregularities visible only by MIM.

The optical patterning of the GST is achieved through shadow-mask patterning with an 800 nm pulsed laser.[27] The mask consists of a 100 nm thick, free-standing gold grating that was fabricated using electron beam lithography and gold electroplating. This free-standing mask was placed on the GST film as an absorptive shadow mask. The areas of the mask with gold absorbed the laser, while the empty areas allowed the laser to interact with the GST.

Topography and MIM were measured for a 400 nm pitch sample, as shown in Figs. 4(b)–4(d). It is immediately obvious from these scans that topography is insufficient to capture all information about where crystallization has occurred. The MIM results uniquely indicate that crystallization in this sample is highly inhomogeneous on the 100s of nm scale. This inhomogeneity likely results from nucleation effects[28] which become relevant at this small length-scale and affects the performance of the devices. It is also possible that inhomogeneous contact between the mask and sample contributes because of diffraction effects behind the mask or inhomogeneous thermal contact to the gold membrane mask, leading to non-uniform loss of heat to the mask during patterning. Mask imperfects are unlikely to contribute. The strong dissipation indicates partial crystallization, in part a result of the need to keep the patterning intensity low enough for the space between lines to remain amorphous.

We have shown the ability of MIM to benefit the characterization of optically patterned PCMs. Conductivity inhomogeneities within spots crystallized by focused lasers can be clearly observed and differences in a thin, oxidized film, where the same full crystallization does not occur. Finally, the ability of MIM to observe electrical inhomogeneity not readily observed by other methods has been demonstrated in optically patterned GST gratings.

MIM holds great promise as a characterization technique for feedback in the fabrication of optically patterned phase change materials and devices, including photonic devices. MIM could also be applied to other PCM devices, including reconfigurable antennas[29] and planar

or cross-sectioned memory cells,[10,30] where MIM may provide the *in-situ* measurement of device operation and degradation.

See supplementary material for the MIM of melted GST, optical methods, and an analysis of the optical intensity required to crystallize the GST films.

This work was partially funded by the NSF under Grant No. DMR1305731 and The Gordon and Betty Moore Foundation, EPiOs under Grant No. GBMF4536, and the DARPA QORS Program. We also thank Kurt Rubin for helpful discussions. Z.-X.S. is a cofounder of PrimeNano Inc., which licensed MIM technology from Stanford for commercial instrumentation. S.W.F. and H.S.P.W. are supported in part by the member companies of the Stanford Non-Volatile Memory Technology Research Initiative (NMTRI).

REFERENCES

[1]H.-S. Wong, S. Raoux, S. Kim, J. Liang, J. P. Reifenberg, B. Rajendran, M. Asheghi, and K. E. Goodson, Proc. IEEE **98**, 2201 (2010).
[2]M. Chen, K. A. Rubin, and R. W. Barton, Appl. Phys. Lett. **49**, 502 (1986).
[3]C. Ríos, P. Hosseini, R. A. Taylor, and H. Bhaskaran, Adv. Mater. **28**, 4720 (2016).
[4]M. Wuttig, H. Bhaskaran, and T. Taubner, Nat. Photonics **11**, 465 (2017).
[5]P. Li, X. Yang, T. W. W. Maß, J. Hanss, M. Lewin, A.-K. U. Michel, M. Wuttig, and T. Taubner, Nat. Mater. **15**, 870 (2016).
[6]S. Raoux, F. Xiong, M. Wuttig, and E. Pop, MRS Bull. **39**, 703 (2014).
[7]K. Lai, H. Peng, W. Kundhikanjana, D. T. Schoen, C. Xie, S. Meister, Y. Cui, M. A. Kelly, and Z. X. Shen, Nano Lett. **9**, 1265 (2009).
[8]P. Zalden, M. J. Shu, F. Chen, X. Wu, Y. Zhu, H. Wen, S. Johnston, Z. X. Shen, P. Landreman, M. Brongersma, S. W. Fong, H. S. P. Wong, M. J. Sher, P. Jost, M. Kaes, M. Salinga, A. Von Hoegen, M. Wuttig, and A. M. Lindenberg, Phys. Rev. Lett. **117**, 067601 (2016).
[9]U. Celano, L. Goux, R. Degraeve, A. Fantini, O. Richard, H. Bender, M. Jurczak, and W. Vandervorst, Nano Lett. **15**, 7970 (2015).
[10]K. Baek, K. Song, S. K. Son, J. W. Oh, S. J. Jeon, W. Kim, H. J. Kim, and S. H. Oh, NPG Asia Mater. **7**, e194 (2015).
[11]M. Lewin, B. Hauer, L. Jung, J. Benke, J. Mayer, M. Wuttig, and T. Taubner, Appl. Phys. Lett. **107**, 151902 (2015).
[12]J.-W. Park, S. H. Eom, H. Lee, J. L. F. Da Silva, Y.-S. Kang, T.-Y. Lee, and Y. H. Khang, Phys. Rev. B **80**, 115209 (2009).
[13]M. Salinga, E. Carria, A. Kaldenbach, M. Bornhöfft, J. Benke, J. Mayer, and M. Wuttig, Nat. Commun. **4**, 2371 (2013).
[14]R. Detemple, I. Friedrich, W. Njoroge, I. Thomas, V. Weidenhof, H.-W. Wöltgens, S. Ziegler, and M. Wuttig, MRS Proc. **674**, V1.8 (2001).
[15]W. K. Njoroge, H.-W. Wöltgens, and M. Wuttig, J. Vac. Sci. Technol. A **20**, 230 (2002).
[16]Y. Yang, K. Lai, Q. Tang, W. Kundhikanjana, M. A. Kelly, K. Zhang, Z.-X. Shen, and X. Li, J. Micromech. Microeng. **22**, 115040 (2012).
[17]K. Lai, W. Kundhikanjana, M. A. Kelly, and Z.-X. Shen, Appl. Nanosci. **1**, 13 (2011).
[18]C. Chen, P. Jost, H. Volker, M. Kaminski, M. Wirtssohn, U. Engelmann, K. Krüger, F. Schlich, C. Schlockermann, R. P. Lobo, and M. Wuttig, Phys. Rev. B **95**, 094111 (2017).
[19]P. I. Lazarenko, A. A. Sherchenkov, S. A. Kozyukhin, A. V. Babich, S. P. Timoshenkov, D. G. Gromov, A. S. Shuliatyev, and E. N. Redichev, AIP Conf. Proc. **1727**, 020013 (2016).
[20]T. Tsafack, E. Piccinini, B.-S. Lee, E. Pop, and M. Rudan, J. Appl. Phys. **110**, 063716 (2011).
[21]H. K. Lyeo, D. G. Cahill, B. S. Lee, J. R. Abelson, M. H. Kwon, K. B. Kim, S. G. Bishop, and B. K. Cheong, Appl. Phys. Lett. **89**, 151904 (2006).
[22]E. Yalon, S. Deshmukh, M. Muñoz Rojo, F. Lian, C. M. Neumann, F. Xiong, and E. Pop, Sci. Rep. **7**, 15360 (2017).
[23]S. Raoux, C. T. Rettner, J. L. Jordan-Sweet, A. J. Kellock, T. Topuria, P. M. Rice, and D. C. Miller, J. Appl. Phys. **102**, 094305 (2007).
[24]E. Gourvest, B. Pelissier, C. Vallée, A. Roule, S. Lhostis, and S. Maitrejean, J. Electrochem. Soc. **159**, 373 (2012).
[25]K. A. Rubin, in *Material Requirements for Reversible Phase Change Optical Recording* (Mater. Res. Soc. Symp. Proc., 1992), Vol. 230, p. 239.
[26]J. Park, P. Zalden, E. Ng, S. Johnston, S. W. Fong, C. Chang, M. Rooks, S. Y. S. Oh, C. J. Tassone, D. Van Campen, H. Mabuchi, H.-S. P. Wong, E. Pop, Z.-X. Shen, A. Lindenberg, and A. Sakdinawat, https://conf-slac.stanford.edu/ssrl-lcls-2015/abstract-details82.html for "X-ray spatial light modulator" (2015).
[27]P. Zalden, A. Von Hoegen, P. Landreman, M. Wuttig, and A. M. Lindenberg, Chem. Mater. **27**, 5641 (2015).
[28]V. Weidenhof, I. Friedrich, S. Ziegler, M. Wuttig, V. Weidenhof, I. Friedrich, S. Ziegler, and M. Wuttig, J. Appl. Phys. **89**, 3168 (2001).
[29]N. Pala, B. Gerislioglu, A. Ahmadivand, and M. Karabiyik, "Phase-change material based reconfigurable antenna," U.S. patent 9923267 (19 Mar 2018).
[30]D. Krebs, S. Raoux, C. T. Rettner, G. W. Burr, R. M. Shelby, M. Salinga, C. M. Jefferson, M. Wuttig, and IBM/Macronix PCRAM Joint Project, J. Appl. Phys. **106**, 054308 (2010).